JACS
JOURNAL OF THE AMERICAN CHEMICAL SOCIETY
Article
pubs.acs.org/JACS

Tungsten Nitrido Complexes as Precursors for Low Temperature Chemical Vapor Deposition of WN_xC_y Films as Diffusion Barriers for Cu Metallization

K. Randall McClain,[†] Christopher O'Donohue,[‡] Arijit Koley,[†] Richard O. Bonsu,[†] Khalil A. Abboud,[†] Joseph C. Revelli,[‡] Timothy J. Anderson,[‡] and Lisa McElwee-White*[,†]

[†]Department of Chemistry, University of Florida, Gainesville, Florida, 32611-7200, United States

[‡]Department of Chemical Engineering, University of Florida, Gainesville, Florida, 32611-6005, United States

Supporting Information

ABSTRACT: Tungsten nitrido complexes of the form $WN(NR_2)_3$ [R = combinations of Me, Et, ^{i}Pr, ^{n}Pr] have been synthesized as precursors for the chemical vapor deposition of WN_xC_y, a material of interest for diffusion barriers in Cu-metallized integrated circuits. These precursors bear a fully nitrogen coordinated ligand environment and a nitrido moiety (W≡N) designed to minimize the temperature required for film deposition. Mass spectrometry and solid state thermolysis of the precursors generated common fragments by loss of free dialkylamines from monomeric and dimeric tungsten species. DFT calculations on $WN(NMe_2)_3$ indicated the lowest gas phase energy pathway for loss of $HNMe_2$ to be β-H transfer following formation of a nitrido bridged dimer. Amorphous films of WN_xC_y were grown from $WN(NMe_2)_3$ as a single source precursor at temperatures ranging from 125 to 650 °C using aerosol-assisted chemical vapor deposition (AACVD) with pyridine as the solvent. Films with stoichiometry approaching W_2NC were grown between 150 and 450 °C, and films grown at 150 °C were highly smooth, with a RMS roughness of 0.5 nm. In diffusion barrier tests, 30 nm of film withstood Cu penetration when annealed at 500 °C for 30 min.

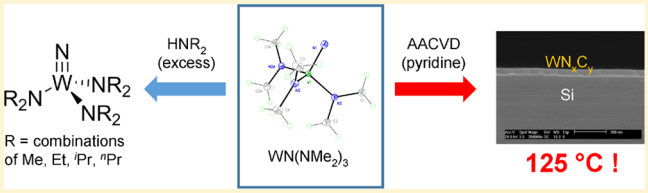

INTRODUCTION

The continuing decrease in microelectronic circuit dimensions has necessitated a shift in interconnect materials to minimize RC (resistance × capacitance) time delay, which has predominantly limited overall device speed. To reduce this time delay, metallization schemes based on aluminum, tungsten, and SiO_2 are being replaced with copper and low-κ (low-dielectric-constant) materials.[1] This transition has generated a need for efficient diffusion barrier materials to prevent destructive interlayer diffusion of copper into adjacent semiconducting and dielectric layers.[2−4] Present Cu interconnect barriers employ a bilayer system composed of a TaN diffusion barrier capped with Ta to promote the adhesion and nucleation of textured Cu.[1] This TaN/Ta bilayer is deposited using PVD (physical vapor deposition) or ionized-PVD, the latter offering advantages in terms of conformality.[5] While advances in this legacy system will likely extend its use, the "line-of-sight" deposition nature of PVD will become prohibitive in increasingly aggressive high aspect ratio features and an eventual transition to a more conformal deposition process, such as CVD (chemical vapor deposition) or ALD (atomic layer deposition), will occur.[6]

Much research has focused on the development of CVD/ALD systems for diffusion barriers based on transition metal nitrides,[7] especially the nitrides of tantalum,[8−16] titanium,[17−23] and tungsten.[24−33] While an effective Cu barrier when deposited via PVD, TaN_x deposition using CVD/ALD generally results in nitrogen rich stoichiometry closer to the high resistivity Ta_3N_5 phase.[12,34−37] Titanium nitride is an effective diffusion barrier and adhesion promoter for Al−Cu and tungsten interconnects but may prove ineffective as a Cu barrier due to its polycrystalline nature that allows diffusion along grain boundaries.[38−40] In addition to metal nitrides, "self-forming" $MnSi_xO_y$ barriers have received recent attention.[41−45] To form these barriers, a Cu−Mn alloy is deposited by PVD or Mn metal is deposited onto the Cu layer via PVD or CVD. Mn then diffuses through Cu to the Cu/dielectric interface during a subsequent annealing step (above 350 °C). The resulting $MnSi_xO_y$ barrier, formed from reaction of Mn with the SiO_2-based dielectric, has a negligible impact on the resistivity of the Cu interconnect because it forms at the surface of the dielectric layer. These highly resistive materials, however, cannot be used as barriers between Cu and semiconducting layers.

WN_x and the ternary material WN_xC_y offer several advantages over other transition metal nitrides as Cu diffusion barriers in terms of resistivity, barrier performance, and processing simplicity.[46] For WN_x, stoichiometry ranging from W_2N to WN has been investigated.[47,48] Tungsten-rich WN_x barriers closer to W_2N have proven to be most desirable due to their lower resistivity and Cu migration rates. Similarly, growth of WN_xC_y films with tungsten-rich stoichiometry approaching W_2NC has resulted in good Cu barriers with low resistivity.[33,49,50]

Received: November 28, 2013
Published: January 2, 2014

   dx.doi.org/10.1021/ja4117582 | J. Am. Chem. Soc. 2014, 136, 1650−1662

Early coreactant systems for deposition of WN_x employed volatile homoleptic tungsten compounds such as WF_6 or $W(CO)_6$ with ammonia as the nitrogen source.[25,27] While cost-effective, these systems generally require high temperature, result in the production of corrosive byproducts, and lead to the incorporation of undesirable impurities in the films. In an effort to alleviate these limitations, much research has focused on tungsten complexes bearing N-coordinated ligands as WN_x/WN_xC_y precursors. These complexes generally contain amide,[26,28,32] imido,[26,28,30,31,36] hydrazido,[33,51] amidinate,[52] and/or guanidinate[53,54] ligands. CVD or ALD using these "metal−organic" WN_x/WN_xC_y precursors, either in single-source mode or in the presence of an appropriate coreactant (usually H_2 or NH_3), has resulted in films virtually free of unsuitable impurities and without the formation of corrosive byproducts.

While several ALD chemistries are reactive enough to allow deposition of WN_x/WN_xC_y at lower temperatures (180−350 °C),[32,55−58] higher temperatures (>350 °C) are generally still required for dissociation of critical bonds during film growth under single source CVD conditions (Table 1). Temperatures above 350 °C can compromise some low-κ materials due to their low thermal stability and can encourage crystallization of barrier materials resulting in low-energy diffusion pathways for Cu migration by grain boundary formation.[2] Design and synthesis of precursors for the deposition of metal nitride films at low temperature (below 350 °C) remain of great interest.[59,60]

Table 1. Minimum Temperature for CVD of WN_xC_y Films from Single Source Precursors

precursor	T (°C)	ref
$Cl_2W(N^tBu)_2(py)_2$	550	61
$W(N^tBu)_2(NH^tBu)_2$	450	25
$Cl_4(CH_3CN)W(N^iPr)$	450	30
$W(N^tBu)_2(NMe_2)\{(^iPr_2N)_2CNMe_2\}$	400	48
$Cl_4(CH_3CN)W(NNMe_2)$	300	62
$WN(NMe_2)_3$	125	*a*

[a]This work.

We previously reported the synthesis and CVD of WN_x nanospheres from $WN(NMe_2)_3$ (**1**) at temperatures as low as 75 °C.[63] We now report the synthesis and characterization of several potential WN_x/WN_xC_y precursors of the general formula $WN(NR_2)_3$ (**2**−**9** and **11**) and describe the deposition of continuous WN_xC_y thin films from **1** at temperatures as low as 125 °C.

RESULTS AND DISCUSSION

Precursor Design. Three of the critical issues in CVD precursor design are minimization of the deposition temperature, the avoidance of deleterious side reactions, and optimization of certain physical properties such as solubility and volatility.[60] In an earlier study involving the kinetics of film growth from the tungsten imido complexes $Cl_4(CH_3CN)W(NR)$ [R = Ph, ^{i}Pr, allyl], correlation of the apparent activation energy for film growth with the bond dissociation energy (BDE) of the N(imido)−C bond implicated cleavage of that bond as the rate determining step for film growth.[31] Modification of the precursor design to replace the critical N(imido)−C bond with a weaker N−N bond resulted in preparation of the hydrazido complexes $Cl_4(CH_3CN)W(NNR_2)$ (R_2 = Me_2, Ph_2, $-(CH_2)_5-$).[62] As predicted from the BDEs, the deposition temperature for $Cl_4(CH_3CN)W(NNMe_2)$ was 300 °C, a drop of 150 °C from that of $Cl_4(CH_3CN)W(N^iPr)$ (Table 1). The next logical step was to eliminate the N-substituent bond by incorporation of a terminal nitrido moiety in **1**.[63] Replacement of the chloride ligands of the earlier imido and hydrazido complexes with dimethylamides in **1** circumvents the formation of the corrosive byproduct HCl, which was observed by mass spectrometry in the reactor effluent from depositions using $Cl_4(CH_3CN)W(NPh)$.[29] By varying the dialkylamido ligands in nitrido complexes **2**−**9** and **11**, the effect of ligand size and branching on pertinent properties, such as volatility and thermal stability, was ascertained.

Precursor Synthesis. After **1** was synthesized in high yield from $WN(O^tBu)_3$ and $Zr(NMe_2)_4$,[63] synthesis of other $WN(NR_2)_3$ complexes from $WN(O^tBu)_3$ was explored. As expected, the reaction of $WN(O^tBu)_3$ with $Zr(NEt_2)_4$ in toluene resulted in complete amide/alkoxide exchange, as observed in the ^{1}H NMR spectra of the product mixture. However, the product, $WN(NEt_2)_3$ (**2**), could not be isolated by selective crystallization or sublimation.

Transamination from **1** using dialkylamines was chosen as a strategy due to the near thermoneutrality of the exchange and the relative volatility of the dimethylamine product. Indeed, reaction of **1** with excess diethylamine (60 equiv) at reflux, either neat or in pentane solution, for 3 h resulted in complete substitution to produce **2**. The crude product was purified easily by recrystallization from hexamethyldisiloxane, resulting in a high yield (85%) of analytically pure **2**.

Scheme 1. Synthesis of 2

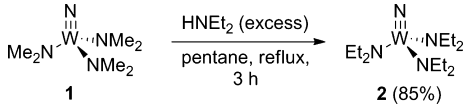

The homoleptic amides $WN(N(Me)Et)_3$ (**3**), $WN(N(Et)^iPr)_3$ (**4**), and $WN(N^nPr_2)_3$ (**5**) were synthesized from **1** by refluxing with a large excess of the appropriate dialkylamine and purified by recrystallization from hexamethyldisiloxane. The reactions were sensitive to the steric demand of the incoming amine, with **4** obtained in refluxing pentane (36 °C), while formation of **5** required refluxing in neat *N*-ethylisopropylamine (71 °C).

Scheme 2. Synthesis of 3−5

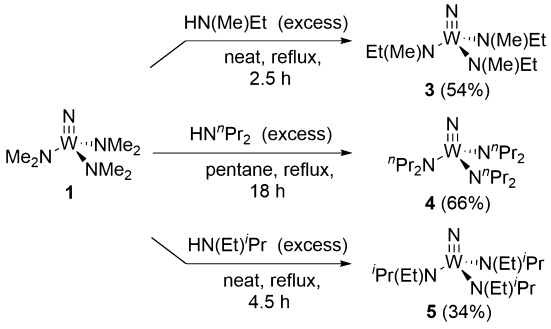

Formation of $WN(N^iPr_2)_3$ could not be achieved by transamination of **1**, even under forcing conditions in neat refluxing diisopropylamine (85 °C). However, $WN(NMe_2)_2(N^iPr_2)$ (**6**) and $WN(NMe_2)(N^iPr_2)_2$ (**7**) were obtained by manipulation of the reaction conditions. Transamination of **1** with excess diisopropylamine in refluxing pentane solution resulted in selective formation of **6**, while conducting the transamination

dx.doi.org/10.1021/ja4117582 | J. Am. Chem. Soc. 2014, 136, 1650−1662

Scheme 3. Synthesis of 6−9

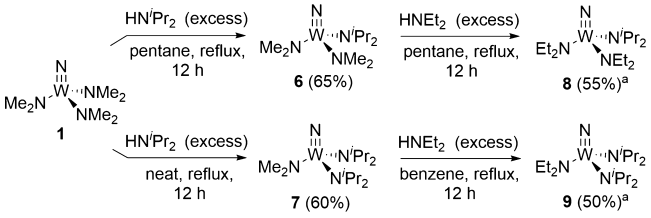

Overall yield from **1**.

of **1** in refluxing diisopropylamine allowed for the selective synthesis of **7**. In both cases, the product could be purified by recrystallization.

The remaining dimethylamide groups of **6** and **7** were cleanly replaced by transamination with excess diethylamine in refluxing pentane or benzene solution to produce WN(NEt$_2$)$_2$(N^{i}Pr$_2$) (**8**) and WN(NEt$_2$)(N^{i}Pr$_2$)$_2$ (**9**), respectively. Analytically pure **8** was obtained by recrystallization from hexamethyldisiloxane, while pure **9** was more efficiently obtained by sublimation owing to its very high solubility. Attempts to generate **8** and **9** by transamination of **2** with diisopropylamine did not result in any significant substitution, even upon reflux in neat diisopropylamine.

WN(N^{i}Pr$_2$)$_3$ (**11**) was eventually synthesized from WN(O^{t}Bu)$_3$ using an alternative two-step procedure. Reaction of WN(O^{t}Bu)$_3$ with La(N^{i}Pr$_2$)$_3$·2THF[64] (0.70 equiv) resulted in amide/alkoxide scrambling to generate WN(O^{t}Bu)(N^{i}Pr$_2$)$_2$ (**10**), which was isolated by sublimation after workup. Reaction of WN(O^{t}Bu)$_3$ or **10** with additional La(N^{i}Pr$_2$)$_3$·2THF did not result in formation of **11**. However, **11** could be obtained by reaction of **10** with excess lithium diisopropylamide in Et$_2$O at 65 °C.

Scheme 4. Synthesis of 10 and 11

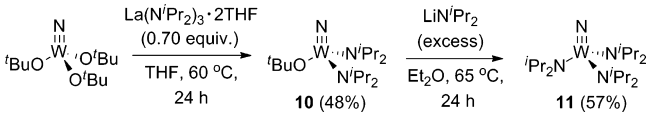

Compounds **2**−**11** were obtained as mostly colorless, air and moisture sensitive crystalline solids after crystallization or sublimation. Samples of the purified **2**−**9** and **11** were sublimed to assay their volatility and stability during gas phase transport (Table 2). Interestingly, compounds **3** and **5**, which contain

Table 2. Sublimation Data for 2, 4, 6−9, and 11

compound	pressure (mTorr)	T (°C)	% recovery
2	150−250	75−80	55
4	150−250	80−90	40
6	350−450	65−70	35
7	350−450	65−70	40
8	250−350	62−68	30
9	250−350	58−68	30
11	100−200	115−125	90

unsymmetrically substituted amide ligands, did not sublime well. Compounds **2**, **4**, and **6**−**9** all sublimed with moderate levels of decomposition (recovery = 30−55%). Compounds **7** and **9** sublimed with higher yield from the crude reaction mixtures than as pure substances. Compound **11** proved to be unique, subliming at higher temperature with excellent thermal stability (recovery = 90%).

Spectroscopic Characterization of 2−11. The ^{1}H and ^{13}C NMR spectra of complexes **2**−**6** and **8** displayed sharp first-order signals indicative of unrestricted rotation about all W−N$_{amide}$ bonds, as found in **1**. The NMR spectra of complexes **7** and **9** exhibited diastereotopic methyl groups on the diisopropylamide ligands. This was evidenced by the appearance of two doublets in the ^{1}H NMR spectra and two closely spaced singlets for the methyl groups in the ^{13}C spectra. The variable temperature ^{1}H NMR spectra of **7** (Figure S-1, Supporting Information) and **9** (Figure S-2, Supporting Information) indicated restricted W−N$_{amide}$ bond rotation at lower temperatures, evidenced by coalescence of the diastereotopic methyl doublets into a broad singlet. The methyl doublets coalesce at −25 and −5 °C for **7** and **9**, respectively. In contrast, the ^{1}H and ^{13}C NMR spectra of compounds **10** and **11** indicated restricted W−N$_{amide}$ bond rotation at room temperature with broad signals for the methyl groups of the diisopropylamide ligands. The behavior of compound **11** is similar to its Cr(VI) analogue CrN(N^{i}Pr$_2$)$_3$, in which restricted Cr−N$_{amide}$ bond rotation was postulated on the basis of NMR results.[65] Variable temperature ^{1}H NMR spectra of **10** (Figure S-3, Supporting Information) and **11** (Figure S-4, Supporting Information) confirmed coalescence of the methyl doublets at 25 °C for both **10** and **11**. Compound **10** displayed four doublets for the methyl protons at low temperature (−45 °C in toluene-d_8) and two doublets for the methyl protons at high temperature (75 °C in benzene-d_6), which is consistent with the presence of diastereotopic methyl groups. It should be noted that the proton signal for the tert-butyl group of **10** remained a sharp singlet at all temperatures, indicating unrestricted W−O bond rotation and weaker π-donor character for this ligand. Compound **11** displayed two doublets for the methyl protons at low temperature (−40 °C in toluene-d_8) and one doublet for the methyl protons at high temperature (75 °C in benzene-d_6).

X-ray Crystal Structure of 7. Complex **7** was chosen for X-ray structure determination because of its heterosubstituted sterically crowded ligand environment and temperature dependent NMR spectra. Crystals suitable for crystallography were grown from concentrated hexamethyldisiloxane solution at low temperature. The asymmetric unit of **7** consists of the three chemically equivalent but crystallographically independent complexes: A, B, and C (Table 3). Accordingly, the following discussion will use bond lengths and angles from complex A unless otherwise specified. As seen in Figure 1, **7** adopts a distorted tetrahedral geometry similar to **1**[63] and **2** (Figure S-5, Supporting Information). The average (A, B, and C) W1—N1 (W≡N) bond length of 1.683(3) in **7** is very similar to that in **1** [W≡N 1.680(2)] and slightly longer than that in WN(N(Ar)^{i}Pr)$_3$[66] (Ar = 3,5-C$_6$H$_3$Me$_2$) [W≡N 1.669(5)]. As in **1**,[63] the W—N$_{amide}$ bond lengths of **7** are shorter [W—N$_{avg}$ 1.953(4)] than those in WN(N(Ar)^{i}Pr)$_3$ (Ar = 3,5-C$_6$H$_3$Me$_2$) [W—N(Ar)^{i}Pr 1.972(3)], a result consistent with the stronger donor (σ, π) character of —NR$_2$ (R = Me, ^{i}Pr)[67] versus —N(Ar)^{i}Pr (Ar = 3,5-C$_6$H$_3$Me$_2$). The total bond angles around N2/N3/N4 in **7** are consistent with sp^2 hybridization [359.9(3), 360.0(3), and 360.1(4)°, respectively], and the amide planes of **7** are parallel to the W≡N axis, allowing π donation into the W based $d_{x^2-y^2}$ and d_{xy} orbitals. A distortion toward trigonal pyramidal geometry is observed in **7**, evidenced by the contraction [{N≡W—N}$_{avg}$, 105.15(16)°] and expansion [{N—W—N}$_{avg}$, 113.42(15)°] of bond angles around W. As in **1**, this is caused by steric repulsion between the more bulky amide groups and a tendency for low overlap between fully occupied bonding orbitals.[68]

dx.doi.org/10.1021/ja4117582 | J. Am. Chem. Soc. 2014, 136, 1650−1662

Table 3. Selected Bond Lengths (Å) and Angles (deg) for 7

W1A–N1A	1.688(3)	N1A–W1A–N3A	104.52(12)
W1B–N1B	1.679(3)	N1B–W1B–N3B	104.50(16)
W1C–N1C	1.681(3)	N1C–W1C–N3C	104.84(16)
W1A–N2A	1.949(3)	N1A–W1A–N4A	105.45(16)
W1B–N2B	1.952(4)	N1B–W1B–N4B	106.20(13)
W1C–N2C	1.957(4)	N1C–W1C–N4C	106.17(12)
W1A–N3A	1.950(3)	N2A–W1A–N3A	113.33(15)
W1B–N3B	1.951(4)	N2B–W1B–N3B	110.87(14)
W1C–N3C	1.955(3)	N2C–W1C–N3C	111.62(15)
W1A–N4A	1.961(4)	N2A–W1A–N4A	113.65(14)
W1B–N4B	1.948(3)	N2B–W1B–N4B	115.00(14)
W1C–N4C	1.945(3)	N2C–W1C–N4C	115.55(14)
N1A–W1A–N2A	105.47(15)	N3A–W1A–N4A	113.29(15)
N1B–W1B–N2B	106.04(15)	N3B–W1B–N4B	113.27(14)
N1C–W1C–N2C	104.95(16)	N3C–W1C–N4C	112.64(15)

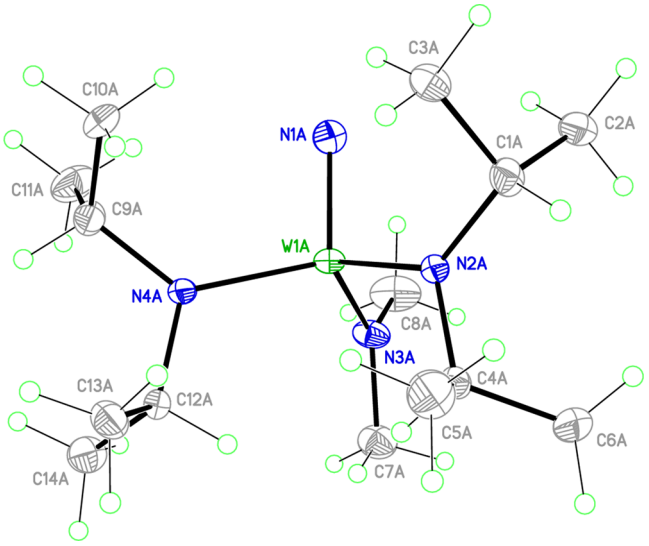

Figure 1. Displacement ellipsoids drawing of **7** (molecule A is shown); ellipsoids are drawn at 50% probability.

Mass Spectrometry. Since the fragmentation patterns observed during mass spectrometry often correlate well with observed CVD decomposition pathways,[31,69,70] the positive ion CI (chemical ionization) mass spectra of compounds **1**–**9** and **11** were obtained (Table 4). For all compounds, the appropriate $[M + H]^+$ ion was observed in high relative abundance, indicating the moderate stability of these thermally sensitive compounds under the ionization conditions. For compounds **1**–**9** and **11**, additional tungsten-containing ions were observed. Some of these fragments correspond to loss of dialkylamine from monomeric $[(M\text{-}HNR_2) + H]^+$ and dimeric $[(M_2\text{-}HNR_2) + H]^+$ species. Both $[(M\text{-}HNR_2) + H]^+$ and $[(M_2\text{-}HNR_2) + H]^+$ ions were clearly evident in the mass spectra of compounds **1**–**4**. Heterosubstituted compounds **6**–**8** generated fragments corresponding to loss of both types of dialkylamines from monomeric and dimeric species, but in most cases (**7**–**9**), the relative abundance of some of the fragments was very low (<1%). However, the mass spectrum of compound **6** clearly displayed all four possible fragments $\{[(M_2\text{-}HNMe_2) + H]^+, [(M_2\text{-}HN^iPr_2) + H]^+, [(M\text{-}HNMe_2) + H]^+, [(M\text{-}HN^iPr_2) + H]^+\}$ with higher relative abundance. Only $[M + H]^+$ and the fragment corresponding to loss of diisopropylamine from a monomeric species $[(M\text{-}HN^iPr_2) + H]^+$ were clearly observed for compound **11**.

Thermolysis of Neat 1 and 2. Thermolyses of **1** and **2** were conducted to identify the volatile byproducts of their thermal decomposition. Neat **1** was heated to 145 °C under 1 atm of Ar, and the volatile products were condensed at −78 °C. ^{1}H NMR and GC-EI-MS analysis of the condensate confirmed the presence of both dimethylamine and trimethylamine. The material remaining after thermolysis was a black powder. Neat **2** was heated to 205 °C under 1 atm of argon, and the volatile products were condensed at −78 °C. ^{1}H NMR, ^{13}C NMR, and GC-EI-MS analysis of the condensate confirmed the presence of diethylamine. The ^{1}H NMR and ^{13}C NMR spectra indicate that a small amount of *N*-ethylethanimine was also present. Again, the material remaining after thermolysis was a black powder.

Computational Study of the Decomposition of 1. Since CI-MS (compounds **1**–**9** and **11**) and thermolysis (compounds **1** and **2**) both indicate formation of dialkylamines during decomposition of $WN(NR_2)_3$ species, a computational study of dialkylamine formation was performed using **1** as a model compound. To investigate the pathway for production of $NHMe_2$

Table 4. Relative Abundances for Positive Ion CI Mass Spectra of Compounds 1–9 and 11

compound (MW)	**selected ions** (*m*/*z*)(*relative abundance*) [formula]
1 (330)	**616**(*31*) $[(M_2\text{-}HNMe_2) + H]^+$; **331**(*95*) $[M + H]^+$; **286**(*7*) $[(M\text{-}HNMe_2) + H]^+$
2 (414)	**756**(*8*) $[(M_2\text{-}HNEt_2) + H]^+$; **415**(*72*) $[M + H]^+$; **342**(*5*) $[(M\text{-}HNEt_2) + H]^+$
3 (372)	**686**(*2*) $[(M_2\text{-}HN(Me)Et) + H]^+$; **373**(*52*) $[M + H]^+$; **314**(*4*) $[(M\text{-}HN(Me)Et) + H]^+$
4 (456)	**826**(*1*) $[(M_2\text{-}HN(Et)^iPr) + H]^+$; **457**(*95*) $[M + H]^+$; **370**(*4*) $[(M\text{-}HN(Et)^iPr) + H]^+$
5 (498)	**896**(*1*) $[(M_2\text{-}HN^nPr_2) + H]^+$; **499**(*12*) $[M + H]^+$
6 (386)	**728**(*26*) $[(M_2\text{-}HNMe_2) + H]^+$; **672**(*11*) $[(M_2\text{-}HN^iPr_2) + H]^+$; **387**(*96*) $[M + H]^+$; **342**(*6*) $[(M\text{-}HNMe_2) + H]^+$; **286**(*2*) $[(M\text{-}HN^iPr_2) + H]^+$
7 (442)	**443**(*23.4*) $[M + H]^+$
8 (442)	**812**(*1*) $[(M_2\text{-}HNEt_2) + H]^+$; **443**(*15*) $[M + H]^+$
9 (470)	**471**(*83*) $[M + H]^+$; **398**(*1*) $[(M\text{-}HNEt_2) + H]^+$; **370**(*2*) $[(M\text{-}HN^iPr_2) + H]^+$
11 (498)	**499**(*52*) $[M + H]^+$; **398**(*1*) $[(M\text{-}HN^iPr_2) + H]$

dx.doi.org/10.1021/ja4117582 | *J. Am. Chem. Soc.* 2014, 136, 1650–1662

Scheme 5. Thermolysis of 1 and 2

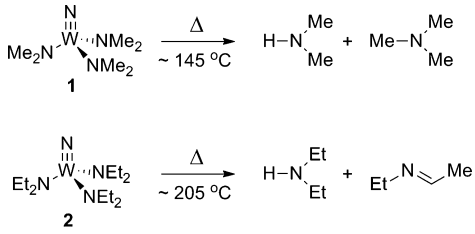

upon thermal decomposition of **1**, two possible decomposition routes were modeled by DFT calculations. In the first (pathway A, Figure 2), the amine arises from an intramolecular β-proton abstraction by one of the amido ligands (via **TS1-A**) to generate a dimethylamine ligand in **INT1-A**, which is displaced upon coordination of a second molecule of **1** (via **TS2-A**) to afford **INT2-A**. In the second pathway (pathway B, Figure 2), dimerization of **1** through a bridging nitrido ligand precedes the proton transfer to generate the amine. The activation energy for the rate determining step in pathway A ($\Delta G^{\ddagger}$ = 49.4 kcal/mol; $\Delta H^{\ddagger}$ = 47.6 kcal/mol via **TS1-A**) is calculated to be significantly higher than that for pathway B ($\Delta G^{\ddagger}$ = 31.0 kcal/mol; $\Delta H^{\ddagger}$ = 14.0 kcal/mol via **TS-B**). These results suggest that decomposition of **1** to release dimethylamine could involve intermolecular interactions in the gas phase above the substrate. Another possibility under deposition conditions is a surface reaction in which coordination of a nitride moiety to an incoming precursor molecule precedes the loss of $NH(CH_3)_2$. The latter is consistent with the formation of dimethylamine during the solid state thermolysis of **1**.

Formation of dimethylamine according to the proposed routes is overall endothermic by approximately 8.2 kcal/mol (ΔG = 24.4 kcal/mol) according to pathway A, or 5.8 kcal/mol (ΔG = 7.7 kcal/mol) according to pathway B. These results are not unreasonable for a reaction occurring under film deposition conditions.

WN_xC_y Film Growth. Pyridine was chosen as the solvent for AACVD because of its stability, appropriate volatility, lack of undesirable elements, and ability to solubilize **1**. To investigate the possibility that pyridine might coordinate to the precursor, pyridine was added to a sample of **1** in benzene-d_6. No evidence of pyridine coordination to **1** was detected in the ^{1}H NMR spectra. Typically, films grown using a solution of **1** in pyridine (0.051 M) under the conditions described in the Experimental Section resulted in film thicknesses less than 100 nm at a substrate temperature as low as 125 °C. Films grown using **1** as a single-source precursor under N_2 ambient adhered to one of two growth regimes, as seen in the Arrhenius plot of growth rate (G) vs reciprocal temperature in Figure 3. The error bars shown in the figure are representative of the film thickness standard deviation near the center of the substrate, for multiple samples and measurements. A small apparent activation energy of 1.39 ± 0.12 kcal/mol (0.056 ± 0.005 eV) is estimated in the low temperature region, 125−400 °C. A similar low activation energy was observed during film growth using the allylimido complex $Cl_4(CH_3CN)W(NCH_2CH{=}CH_2)$ (0.15 eV).[31] The allylimido complex is expected to have a higher activation energy for film growth than that of **1**, due to the presence of the imido substituent (see the Precursor Design section). This low apparent activation energy is consistent with mass transfer limited growth, which shows a T^n temperature dependence, where n is dependent on the reactor design (e.g., n = 1.5 for a horizontal reactor).[31,71−73] The temperature dependence of film growth rate in the low-temperature regime was estimated as $T^{1.32}$. Moreover, there was no growth rate dependence on the substrate orientation (i.e., p-type boron-doped Si(100) and n-type arsenic-doped Si(111)), which further supports mass transfer limited growth.

The maximum growth rate observed in the low-temperature regime was 4.9 Å/min at a deposition temperature of 400 °C, whereas the minimum growth rate was 2.3 Å/min at 125 °C. These growth rates are less than that of typical CVD growth rates,[74] which supports the possibility that the rate determining step is bimolecular, consistent with the location of lower energy transition states for amine loss by DFT (Figure 2).

At higher temperature, >400 °C, the growth rate decreases with increasing temperature with an apparent activation energy of −9.37 ± 0.22 kcal/mol (−0.386 ± 0.008 eV). This regime exhibits an abrupt onset, occurring at 450 °C, and falls to 0.3 Å/min at 650 °C. The decreasing-growth-rate regime is likely dominated by premature and aggressive gas-phase reactions upstream of the substrate, desorption of adatoms from the surface, or a combination of the two. Parasitic homogeneous reaction of **1** is evidenced by the observation of wall deposition upstream of the heated susceptor, no measurable dependence of growth rate on the Si substrate orientation, as well as a significant increase in carbon content in the films, which is most likely from incorporation of byproducts from upstream reactions.

WN_xC_y Film Microstructure. For barrier films, an amorphous microstructure is more desirable than a polycrystalline one because amorphous materials offer no low-energy diffusion pathways, such as grain boundaries, for Cu migration.[4] It should be noted that depositions using **1** as a single-source precursor yield highly amorphous thin films with no detectable crystallinity (Figure 4A) within the relatively large temperature range 125−650 °C. Figure 4A depicts a 2θ scan for the lowest (125 °C), highest (650 °C), and intermediate (350 °C) deposition temperatures, and clearly shows the amorphous nature of the films per the absence of any crystallographic peaks (as compared to the dominant reflections for powders indicated by the stick pattern in Figure 4B). On the basis of previous work using other precursors, the primary β-WN_xC_y reflections are expected to result from a solid solution of β-W_2N and β-WC_{1-x} and that their respective reflections are very approximate to each other, hence illustrated as a single reflection. The appropriate crystallographic planes are labeled for these reflections, and they correspond to the planes of both β-W_2N and β-WC_{1-x} solutions. Similarly, the primary WO_3 pattern is an amalgamation of reflections for three common WO_3 phases: cubic, tetragonal, and monoclinic.

WN_xC_y Film Composition. X-ray photoelectron spectroscopy (XPS) was used to quantify atomic composition in the film and to establish the valence states of each element in the film. Figure 5 shows the atomic concentration in the films versus deposition temperature. Only four elements were present in the film: W, C, N, and O. The error bars represent a sensitivity of one atomic percent for the instrument used.

In the deposition temperature range 150−450 °C, the film composition was relatively constant with average atomic percent values of 41, 13.6, 13.6, and 31.5% for W, N, C, and O, respectively. This results in a film consisting of WO_3 and the carbonitride phase $WN_{0.45}C_{0.45}$. Typically, WN_xC_y films where x and $y \approx 0.5$ provide the lowest resistivity and highest Cu migration resistance.

dx.doi.org/10.1021/ja4117582 | J. Am. Chem. Soc. 2014, 136, 1650−1662

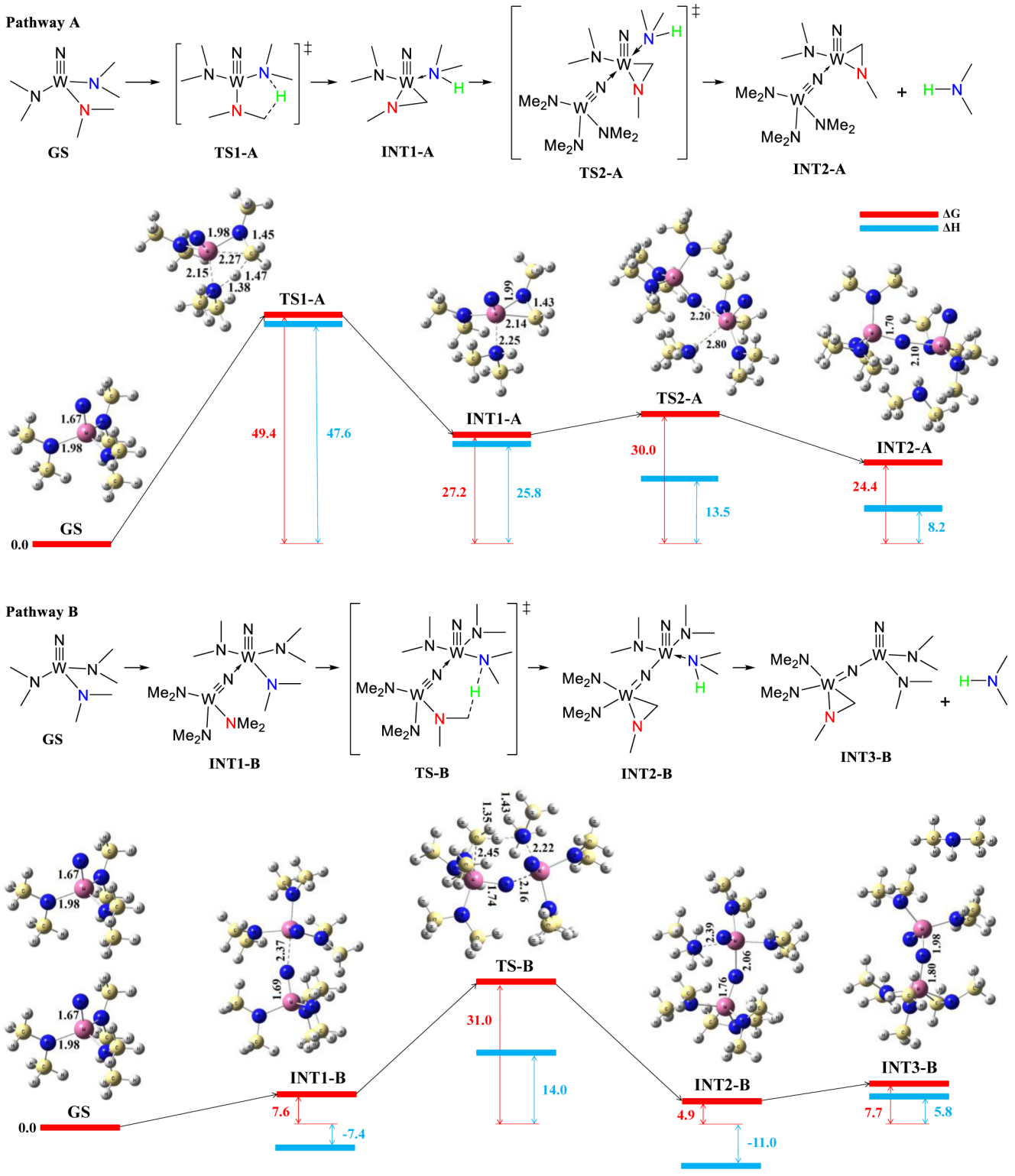

Figure 2. Energy profiles (ΔG and ΔH, in kcal mol^{-1}) and bond lengths (Å) for pathway **A** involving initial unimolecular β-proton abstraction by amide and pathway **B** involving initial bimolecular β-proton abstraction by amide. Calculations performed at the M06L/LanL2DZ/6-31G* level in the gas phase at room temperature.

There is a noticeable change in composition for films grown above 550 °C and below 150 °C. Above 550 °C, the change is most likely caused by upstream gas phase decomposition of both precursor and solvent.[75] A dramatic increase in C and a sharp decrease in W are consistent with solvent decomposition and/or precursor disappearance by parasitic reaction. Incorporation of oxygen in the film is reduced by the stuffing of carbon into the film. Below 150 °C, it is likely that the precursor does not decompose fully and ligands are incorporated into the film. At these low temperatures, the sticking probability of gaseous molecules is high[76] and any background oxygen or water vapor is likely integrated into the film.

dx.doi.org/10.1021/ja4117582 | J. Am. Chem. Soc. 2014, 136, 1650−1662

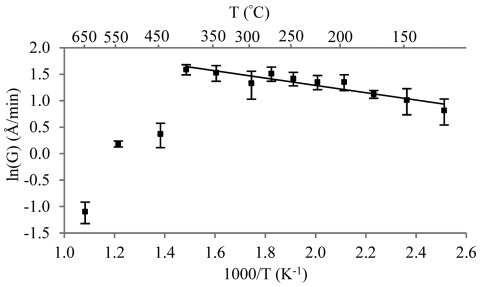

Figure 3. Arrhenius plot of growth rate (G) for films deposited with **1** depicting the two well-defined growth regimes.

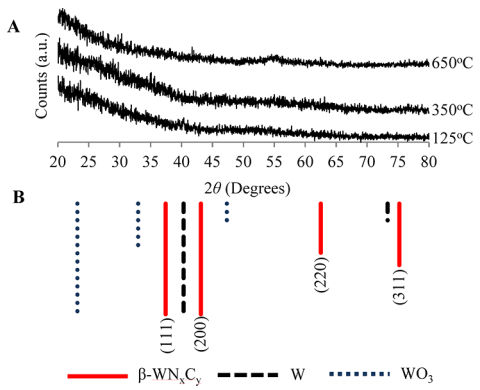

Figure 4. (A) Grazing incidence X-ray diffraction (GIXRD) patterns taken for films deposited using compound **1**. (B) Typical crystallographic planes for relevant materials with respect to their preferred structures and according to their relative intensities.

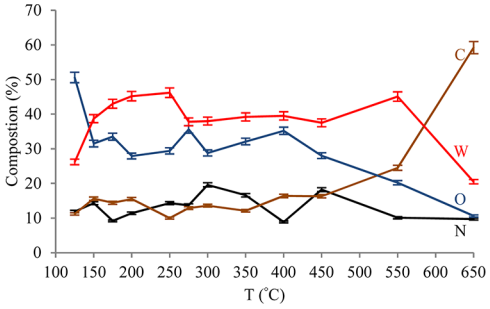

Figure 5. Atomic composition of films as a function of deposition temperature as determined by XPS.

Figure 6 illustrates the evolution of the primary elemental peaks in the XPS spectra of films grown at various deposition temperatures. With increasing deposition temperature, the W 4f peak shifted from higher binding energies (BEs) to lower ones, suggesting a transition from a higher oxidation state to a lower one. Typical BEs for tungsten oxide, WO_3, reside around 35.7 and 37.7 eV for the W $4f_{7/2}$ and W $4f_{5/2}$ peaks, respectively. Typical BEs for WN_xC_y reside around 32.1 and 34.1 eV for the W $4f_{7/2}$ and W $4f_{5/2}$ peaks, respectively.[77] W 4f peaks for WC_{1-x} and WN_x are separated by 0.2 eV and are generally considered indistinguishable, so a single peak for WN_xC_y was assumed. It can be seen that as deposition temperature increases W becomes predominately bound as a WN_xC_y solid solution.

Deconvolution of the W 4f peak for the sample grown at 125 °C suggests that approximately 60% of the W is bound to O. For the film at the 250 °C growth temperature, the oxide peaks shift 0.5 to 35.2 and 37.2 eV (i.e., lower BE) for the W $4f_{7/2}$ and

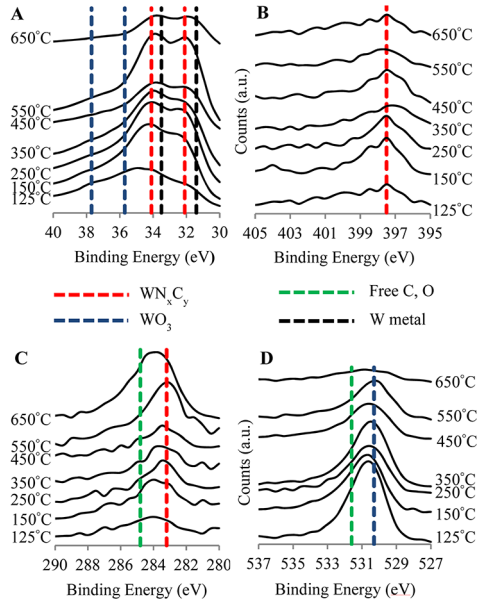

Figure 6. Peak evolution with deposition temperature for primary peaks (A) W 4f, (B) N 1s, (C) C 1s, and (D) O 1s. The superimposed stick patterns identify typical BEs[77] for relevant valence states associated with each respective element.

W $4f_{5/2}$ peaks, respectively. This implies a reduction of W, most likely to an oxide solid solution of WO_3 and WO_2, as WO_x. The percentage of the W signal in the oxide state, however, is reduced to about 25% with the balance consistent with a WN_xC_y solid solution. The W 4f peak for the sample grown at the highest temperature (650 °C) indicates 85% of the W resides in a WN_xC_y energy state, with only about 15% of the W signal existing in a slightly more reduced (0.8 eV negative shift) WO_x form.

The N 1s peak position is consistently at a BE of 397.5 eV for all deposition temperatures except 125 °C, implying it is W bound. CN_x can invoke multiple BEs for the N 1s peak depending on the nature of the film, but these typically range from 398.5 to 400.6 eV. Deconvolution of the peak for the film deposited at 125 °C generated two distinct peaks, one at 400.1 eV (~30% of the N signal), corresponding to CN_x, and the other at 397.5 eV, corresponding to WN_x.

The C 1s peak is nominally located at 283.5 eV in WN_xC_y, 284.5 eV as amorphous C, and 286 eV in CN_x. Only films deposited at 125 °C yielded a C 1s peak located at 286 eV (285.9 eV) (~30% of the C signal), which is consistent with the N 1s data. Growth temperatures from 150 to 275 °C produced films almost entirely (85%) in a carbidic state. At intermediate temperatures (300 °C < T < 500 °C), the carbon predominantly resided in a carbidic (~90%) state, with the balance as amorphous carbon. Above 550 °C, the amorphous carbon content increased linearly until 650 °C to a maximum 45%, balanced by 55% carbidic C. An increase in free C is expected with increasing deposition temperature, since solvent decomposition is more likely. It appears that growing at 125 °C resulted in incomplete pyrolysis of **1**, which is evident in both the C 1s and N 1s peaks.

Oxygen is an impurity in the film and is likely incorporated by post-growth exposure to air and/or residual oxygen and water vapor in the reactor during film growth. Due to the amorphous nature and low density of the films, significant in-diffusion of oxygen is possible post-growth. The background O-source partial pressure was estimated to be ~35 mTorr (~0.0001 mol fraction).

dx.doi.org/10.1021/ja4117582 | J. Am. Chem. Soc. 2014, 136, 1650−1662

O levels in the films reduce at higher growth temperature because of sufficient thermal budget to replace O with C in the crystal lattice, as well as the inhibition of post-growth incorporation due to C stuffing in the lattice. The O 1s peak for adsorbed oxygen is positioned at 531.6 eV, whereas those for WO_3 and WO_2 are approximately 530.5 and 530.4 eV, respectively, so for simplicity, they are considered as a single peak. At temperatures less than 300 °C, the O is bound nearly equally, 55 and 45%, as adventitious oxide and WO_x, respectively. At temperatures above 300 °C, the O signal is increasingly consistent with the BE of WO_x (58%), whereas the adventitious oxide contribution is reduced to 42%.

It has been reported that using H_2 or a H_2/NH_3 as a carrier gas reduces O incorporation.[51,61,78,79] Unfortunately, film growth proved to be difficult under those conditions due to stable precursor transport issues.

WN_xC_y Film Surface Roughness. Films deposited using **1** resulted in smooth films with root-mean-squared (RMS) roughness values on average below 2.5 nm. At lower temperatures, the roughness is near that of the underlying Si substrate (1.8 Å), as can be seen in Figure 7A. The sharp increase in roughness at 175 °C could be indicative of a Stranski−Krastanov growth mechanism, upon transitioning from a two-dimensional to a three-dimensional growth. It has been shown that WN_x films undergo compressive stresses, which facilitates island formation. The surface roughness displayed an approximately linear correlation to growth rate from 125 to 350 °C. This most likely is the result of insufficient energy for adsorbed species (adatoms) to overcome the surface diffusion barrier,[80] so the increasing growth rate propagates underlying features more quickly.[81] Between 350 and 450 °C, the surface roughness becomes nearly constant, which is the result of adatom mobility saturation.[80] At higher temperatures, the surface mobility barrier is nonexistent, which allows for the smoothing of films,[82] as can be seen from 450 to 650 °C. This relatively smooth surface promotes strong adhesion to neighboring layers and limits the amount of interfacial resistance due to electron scattering, which is especially important to low resistance Cu contacts[83,84] in devices.

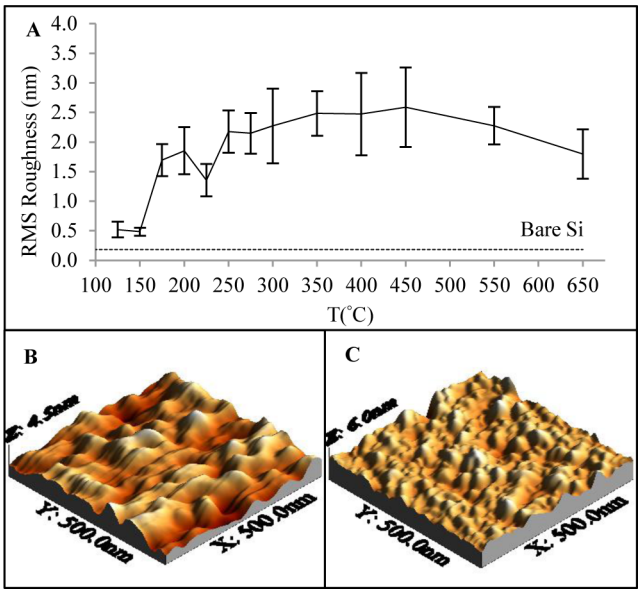

Figure 7. (A) Average surface roughness for films deposited from **1** at different deposition temperatures (black). The dotted horizontal line is the RMS roughness of the underlying bare Si. (B) Atomic force microscopy (AFM) micrograph for films deposited from **1** at 150 °C. (C) AFM micrograph for films deposited from **1** at 550 °C.

WN_xC_y Film Density Measurements. Films deposited using **1** were analyzed with X-ray reflectivity (XRR) to determine film densities as a function of deposition temperature. Figure 8 depicts this dependency and clearly shows film densification with increasing deposition temperature, except at 650 °C. This is typical of CVD type growth as transport rates in the solid increase,[80,81] which facilitates increased crystallinity. Density decreases at 650 °C when large amounts of amorphous C are incorporated into the film. Amorphous C has a density[85] between 2 and 3 g/cm^3, consistent with a decrease in film density upon mixing with WN_xC_y. Typical bulk values for crystalline WN_xC_y have been reported[86] at approximately 15.6 g/cm^3, whereas bulk values for amorphous WN_xC_y have been reported[87−89] between 3 and 13.1 g/cm^3. The relatively deflated density values can be attributed to oxygen incorporation, which enhances the disorder in the film. Despite the relatively low density values, it has been shown that film microstructure is of more importance than film density for diffusion barrier applications.[90]

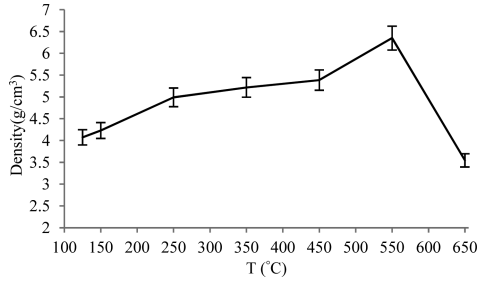

Figure 8. Correlation between deposition temperature and measured film density.

Diffusion Barrier Tests. The integrity of the films as diffusion barriers was evaluated by depositing approximately 300 nm of Cu (according to the Experimental Section) onto 30 nm (per CS-SEM) of WN_xC_y film and annealing the Cu/WN_xC_y/Si stack at 500 °C for 30 min. To detect large-scale diffusion of Cu through the barriers, XRD and four point probe (4PP) measurements were performed. Figure 9 illustrates the changes in crystallinity between pre- and post-annealing of

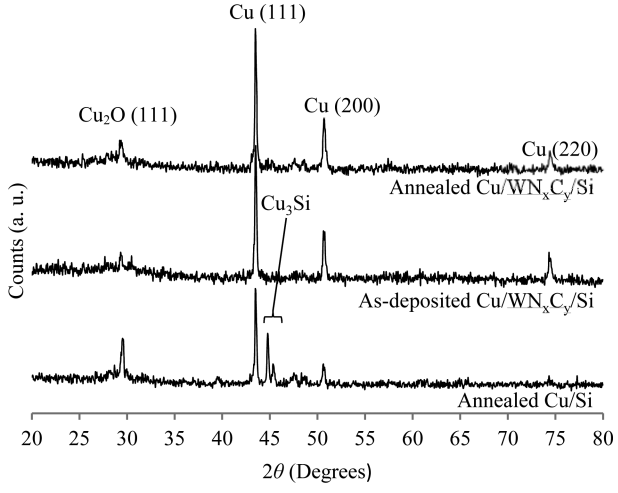

Figure 9. XRD patterns depicting the crystallinity for pre- and post-annealed Cu/WN_xC_y/Si material stacks with an annealed Cu/Si stack as reference.

dx.doi.org/10.1021/ja4117582 | J. Am. Chem. Soc. 2014, 136, 1650−1662

the samples. Peaks for Cu(111), Cu(200), and Cu(220) are evident at 43.47, 50.65, and 74.28 $2\theta^{\circ}$, respectively. Cu(111) is the preferred orientation for barrier applications, since it offers the lowest electrical resistivity and highest electromigration resistance.[4,91] The ratio of the two most common peaks, Cu(111) to Cu(200), is approximately 5:3, which increases to 5:2 with annealing. These ratios are consistent with other reports for deposition of Cu by MOCVD.[92,93] The Cu_2O peak that appears during the annealing process results from background oxygen and water vapor in the deposition chamber. The critical peaks are the Cu_3Si (110) and Cu_3Si (103) peaks that appear at 44.75 and 45.30 $2\theta^{\circ}$, respectively, in the annealed Cu/Si stack but do not appear in either the pre- or post-annealed $Cu/WN_xC_y/Si$ stacks. These results indicate that barrier integrity was maintained.

The onset of Cu_3Si precipitates can drastically increase the resistivity of the material stacks, as observed in the Cu/Si stack upon annealing. The as-deposited and annealed Cu/Si stack had resistivity measurements of 5.4 ± 0.7 and 384 ± 5.7 $\mu\Omega$-cm, respectively. In contrast, the resistivity values of the as-deposited and annealed $Cu/WN_xC_y/Si$ stacks were 6.8 ± 0.3 and 6.3 ± 0.4 $\mu\Omega$-cm, respectively, which is consistent with no Cu diffusion through the barrier film. The slight difference in resistivity between the as-deposited $Cu/WN_xC_y/Si$ and Cu/Si stacks can be attributed to the more resistive barrier film (vs Cu) as well as interfacial resistance.

An etch-pit test was also performed to provide insight into small-scale Cu diffusion through the barrier. This method is generally considered more sensitive than either resistivity or XRD measurements. Figure 10 displays SEM plan-view images of

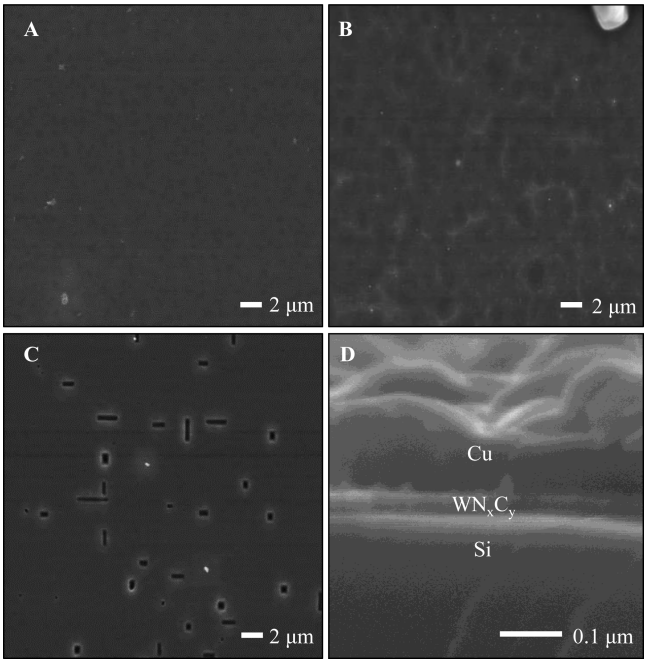

Figure 10. (A) Plan-view of etch-pit test for pre-annealed $Cu/WN_xC_y/Si$ stack, (B) plan-view of etch-pit test for post-annealed $Cu/WN_xC_y/Si$ stack, and (C) plan-view of etch-pit test of a failed barrier for comparison purposes. (D) Cross-sectional view of post-annealed $Cu/WN_xC_y/Si$ stack.

etched films on both the pre- (Figure 10A) and post-annealed $Cu/WN_xC_y/Si$ stacks (Figure 10B), in addition to a cross-sectional image of a post-annealed $Cu/WN_xC_y/Si$ stack showing the intact barrier (Figure 10D). In the event of barrier failure, micrometer-sized inverted pyramidal features (appearing as dark rectangles in Figure 10C) would be visible on the surfaces in the plan-view images. The lack of inverted pyramidal features in Figure 10A and B is more sensitive evidence for successful barrier performance during annealing.

CONCLUSION

In conclusion, we have prepared tungsten nitrido complexes of the type $WN(NR_2)_3$ [**1**–**9** and **11**; R = combinations of Me, Et, ^{i}Pr, ^{n}Pr] as single source precursors for the deposition of WN_xC_y films. Inclusion of the terminal nitrido ligand in place of the imido or hydrazido ligands in previously reported precursors dramatically lowered the film deposition temperature to 125 °C. $WN(NMe_2)_3$ (**1**) proved to be a viable precursor for the deposition of robust WN_xC_y thin films for Cu diffusion barrier purposes at very low growth temperatures. Further investigation of barrier materials grown from complexes **2**–**9** and **11** is currently underway.

EXPERIMENTAL SECTION

General Procedures. Unless otherwise specified, all manipulations were performed under an inert atmosphere (N_2, Ar) using standard Schlenk and glovebox techniques. Toluene, benzene, and hexane were purified using an MBraun MB-SP solvent purification system and stored over activated 3 Å molecular sieves prior to use. Diethyl ether and tetrahydrofuran were dried using sodium/benzophenone, distilled, and stored over activated 3 Å molecular sieves prior to use. Benzene-d_6, toluene-d_8, and THF-d_8 were purchased from Cambridge Isotope Laboratories, Inc., and stored over activated 3 Å molecular sieves (15% w/v) for several days in an inert atmosphere glovebox prior to use. Anhydrous *tert*-butanol, pentane, and redistilled diisopropylamine were purchased from Sigma-Aldrich and used as received. Anhydrous 1,2-dimethoxyethane, diglyme, and pyridine were purchased from Sigma-Aldrich and stored over activated 3 Å molecular sieves for several days in an inert atmosphere glovebox prior to use. Hexamethyldisiloxane, diethylamine, dipropylamine, *N*-ethylmethylamine, and *N*-ethylisopropylamine were purchased from Sigma-Aldrich or Alfa Aesar and stored over activated 3 Å molecular sieves (15% w/v) for several days in an inert atmosphere glovebox prior to use. Solid lithium diisopropylamide was prepared from the reaction of butyllithium (1.6 M in hexanes) and excess diisopropylamine (1.25 equiv.) and used shortly after preparation. $La(N^{i}Pr_2)_3{\cdot}2THF$[64] was prepared using published methods. $WN(O^{t}Bu)_3$ and **1** were prepared by modified procedures (Supporting Information) adapted from a previous publication.[63] All other chemicals were purchased and used as received. ^{1}H and ^{13}C NMR spectra were obtained using Gemini, Mercury, or VXR 300 MHz spectrometers (Varian shims/probes; Oxford magnets) using the residual protons of the deuterated solvents as reference peaks. Mass spectra were obtained with a Thermo Scientific Trace GC DSQ mass spectrometer using the DIP-CI mode of operation. Elemental analysis results were attained from Complete Analysis Laboratories, Inc.

*$WN(NEt_2)_3$ (**2**).* In a 100 mL Schlenk flask, 2.22 g (6.72 mmol) of **1** and 40 mL of pentane were combined to create a white slurry. To the slurry, 21 mL of diethylamine (15 g, 200 mmol) was added all at once to give an orange/red suspension. A reflux condenser was attached, and the reaction mixture was brought to a gentle reflux under argon. After 3 h, the resulting light amber solution was returned to room temperature and all volatiles were removed under vacuum. The remaining rusty/tan residue was extracted by stirring with hexamethyldisiloxane (10 mL) for 15 min and filtered through Celite. The filter pad was washed with additional hexamethyldisiloxane (2 × 5 mL). The resulting amber filtrate was concentrated to saturation under vacuum and placed in the glovebox refrigerator (−15 °C) overnight. The mother liquor was removed, and the pure product was dried under vacuum to yield 2.37 g (5.72 mmol) of pure **2** as white needle-like crystals (85%). ^{1}H NMR (C_6D_6, 300 MHz): $\delta = 1.16$ [t, $J = 7$ Hz, 18 H, $-N(CH_2CH_3)_2$]; 3.58 [q, $J = 7$ Hz, 12 H, $-N(CH_2CH_3)_2$]. ^{13}C NMR (C_6D_6, 300 MHz): $\delta = 17.8$

dx.doi.org/10.1021/ja4117582 | J. Am. Chem. Soc. 2014, 136, 1650−1662

[−N(CH$_2$CH$_3$)$_2$]; 52.6 [−N(CH$_2$CH$_3$)$_2$]. DIP-CI-MS: calcd for [M + H]$^+$ 415.2060; found 415.2062. $C_{12}H_{30}N_4W$ (414.24): calcd C 34.79, H 7.30, N 13.53; found C 34.76, H 7.19, N 13.60.

*WN(N(Me)Et)$_3$ (**3**).* In a 10 mL Schlenk flask, 0.25 g (0.76 mmol) of WN(NMe$_2$)$_3$ and 3.0 mL of *N*-ethylmethylamine (2.1 g, 35 mmol) were combined to create an orange/red suspension. A reflux condenser was attached, and the reaction mixture was brought to a gentle reflux under argon. After 2.5 h, the resulting orange/amber solution was returned to room temperature and all volatiles were removed under vacuum. The rusty/tan residue was extracted by stirring with excess pentane (7 mL) for 15 min and filtered through Celite. The filter pad was washed with additional pentane (2 × 3 mL). All volatiles were removed from the resulting amber filtrate under vacuum. The crude product was dissolved in minimal hexamethyldisiloxane, concentrated to saturation, and placed in the glovebox refrigerator (−15 °C) overnight. The mother liquor was removed, and the product was dried under vacuum to yield 0.15 g (0.40 mmol) of pure **3** as a tan microcrystalline powder (53%). ^{1}H NMR (C$_6$D$_6$, 300 MHz): δ = 1.11 [t, J = 7 Hz, 9 H, −NCH$_3$(CH$_2$C*H*$_3$)]; 3.35 [s, 9 H, −NC*H*$_3$(CH$_2$CH$_3$)]; 3.58 [q, J = 7 Hz, 6 H, −NCH$_3$(C*H*$_2$CH$_3$)]. ^{13}C NMR (C$_6$D$_6$, 300 MHz): δ = 17.0 [−NCH$_3$(CH$_2$*C*H$_3$)]; 47.3 [−NCH$_3$(CH$_2$*C*H$_3$)]; 57.4 [−NCH$_3$(*C*H$_2$CH$_3$)]. DIP-CI-MS: calcd for [M + H]$^+$ 373.1584; found 373.1599. $C_9H_{24}N_4W$ (372.16): calcd C 29.05, H 6.50, N 15.05; found C 28.91, H 6.43, N 15.01.

*WN(N(Et)^{i}Pr)$_3$ (**4**).* In a 25 mL Schlenk flask, 0.21 g (0.64 mmol) of **1** and 4.0 mL (2.9 g, 33 mmol) of *N*-ethylisopropylamine were combined to give an orange/red suspension (some white precipitate). A reflux condenser was attached, and the reaction mixture was brought to a gentle reflux under argon. After 4.5 h, the resulting dark brown solution was returned to room temperature and all volatiles were removed under vacuum to leave a tan/brown solid residue. The residue was extracted by stirring with hexamethyldisiloxane (5 mL) for 15 min and filtered through Celite. The filter pad was washed with additional hexamethyldisiloxane (2 × 3 mL). The resulting dark amber filtrate was concentrated to saturation under vacuum and placed in the glovebox refrigerator (−15 °C) overnight. The mother liquor was removed, and the product was dried under vacuum to yield crude **4** as a light brown powder (mostly pure by ^{1}H NMR). The product was recrystallized with minimal hexamethyldisiloxane to yield 0.10 g (0.22 mmol) of pure **4** as a light brown microcrystalline powder (34%). ^{1}H NMR (C$_6$D$_6$, 300 MHz): δ = 1.05 [t, J = 7 Hz, 9 H, −NCH$_2$C*H*$_3$(CH(CH$_3$)$_2$)]; 1.45 [d, J = 7 Hz, 18 H, −NCH$_2$CH$_3$(CH(C*H*$_3$)$_2$)]; 3.20 [q, J = 7 Hz, 6 H, −NC*H*$_2$CH$_3$−(CH(CH$_3$)$_2$)]; 3.32 [m, J = 7 Hz, 3 H, −NCH$_2$CH$_3$(C*H*(CH$_3$)$_2$)]. ^{13}C NMR (C$_6$D$_6$, 300 MHz): δ = 19.0 [−NCH$_2$*C*H$_3$(CH(CH$_3$)$_2$)]; 27.2 [−NCH$_2$CH$_3$(CH(*C*H$_3$)$_2$)]; 49.1 [−N*C*H$_2$CH$_3$(CH(CH$_3$)$_2$)]; 56.8 [−NCH$_2$CH$_3$(*C*H(CH$_3$)$_2$)]. DIP-CI-MS: calcd for [M + H]$^+$ 457.2524; found 457.2516. $C_{15}H_{36}N_4W$ (456.32): calcd C 39.48, H 7.95, N 12.28; found C 39.42, H 7.86, N 12.19.

*WN(N^{n}Pr$_2$)$_3$ (**5**).* In a 25 mL Schlenk flask, 0.25 g (0.76 mmol) of **1** and 12 mL of pentane were combined to create a white slurry. To the slurry, 3.0 mL of dipropylamine (2.2 g, 22 mmol) was added all at once to give an orange/red suspension. A reflux condenser was attached, and the reaction mixture was brought to a gentle reflux under argon. After 18 h, the resulting orange/red solution was returned to room temperature and all volatiles were removed under vacuum to leave a tan solid residue. The residue was extracted by stirring with hexamethyldisiloxane (7 mL) for 15 min and filtered through Celite. The filter pad was washed with additional hexamethyldisiloxane (2 × 3 mL). The resulting amber filtrate was concentrated to saturation under vacuum and placed in the glovebox refrigerator (−15 °C) overnight. The mother liquor was removed, and the pure product was dried under vacuum to yield 0.25 g (0.50 mmol) of pure **5** as off-white needles (66%). ^{1}H NMR (C$_6$D$_6$, 300 MHz): δ = 0.90 [t, J = 7 Hz, 18 H, −N(CH$_2$CH$_2$C*H*$_3$)$_2$]; 1.64 [m, J = 7 Hz, 12 H, −N(CH$_2$C*H*$_2$CH$_3$)$_2$]; 3.62 [t, J = 7 Hz, 12 H, −N(C*H*$_2$CH$_2$CH$_3$)$_2$]. ^{13}C NMR (C$_6$D$_6$, 300 MHz): δ = 12.0 [−N(CH$_2$CH$_2$CH$_3$)$_2$]; 25.1 [−N(CH$_2$CH$_2$CH$_3$)$_2$]; 61.1 [−N(CH$_2$CH$_2$CH$_3$)$_2$]. DIP-CI-MS: calcd for [M + H]$^+$ 499.3000; found 499.2991. $C_{18}H_{42}N_4W$ (498.40): calcd C 43.38, H 8.49, N 11.24; found C 43.26, H 8.39, N 11.13.

*WN(NMe$_2$)$_2$(N^{i}Pr$_2$) (**6**).* In a 100 mL Schlenk flask, 0.25 g (0.76 mmol) of **1** and 60 mL of pentane were combined to create a white slurry. To the slurry, 3.0 mL of diisopropylamine (2.2 g, 21 mmol) was added to give an orange/red suspension. A reflux condenser was attached and the mixture was brought to a gentle reflux under argon. After 12 h, the resulting amber/brown solution was returned to room temperature and solvent was removed under vacuum. The product was extracted by stirring with hexamethyldisiloxane (30 mL) for 15 min and filtered through Celite. The filter pad was washed with additional hexamethyldisiloxane (2 × 5 mL). The resulting brown filtrate was concentrated to saturation and left in the glovebox refrigerator (−15 °C) overnight. The mother liquor was removed, and the product was dried under vacuum to yield 0.19 g (0.49 mmol) of pure **6** as colorless microcrystals (65%). ^{1}H NMR (C$_6$D$_6$, 300 MHz): δ = 1.31 [d, J = 6 Hz, 12 H, −N(CH(C*H*$_3$)$_2$)$_2$]; 3.35 [s, 12 H, −N(C*H*$_3$)$_2$]; 3.41 [m, J = 6 Hz, 2 H, −N(C*H*(CH$_3$)$_2$)$_2$]. ^{13}C NMR (C$_6$D$_6$, 300 MHz): δ = 26.4 [−N(CH(*C*H$_3$)$_2$)$_2$]; 51.3 [−N(*C*H$_3$)$_2$]; 51.9 [−N(*C*H(CH$_3$)$_2$)$_2$]. DIP-CI-MS: calcd for [M + H]$^+$ 387.1747; found 387.1750. $C_{10}H_{26}N_4W$ (386.19): calcd C 31.10, H 6.79, N 14.51; found C 30.93, H 6.83, N 14.43.

*WN(NMe$_2$)(N^{i}Pr$_2$)$_2$ (**7**).* In a 100 mL Schlenk flask, 0.50 g (1.5 mmol) of **1** and 10 mL of diisopropylamine (7.2 g, 71 mmol) were combined to give an orange/red suspension. A reflux condenser was attached, and the mixture was brought to a gentle reflux under argon. After 12 h, solvent was removed from the dark brown solution under vacuum at room temperature. The crude product was extracted by stirring with hexamethyldisiloxane (50 mL) for 15 min and filtered through Celite. The filter pad was washed with additional hexamethyldisiloxane (2 × 5 mL). The resulting brown filtrate was concentrated to saturation and left in the glovebox refrigerator (−15 °C) overnight. The mother liquor was removed, and the product was dried under vacuum to yield 0.40 g (0.90 mmol) of pure **7** as colorless microcrystals (60%). ^{1}H NMR (C$_6$D$_6$, 300 MHz): δ = 1.29 [d, J = 6 Hz, 12 H, −N(CH(C*H*$_3$)$_a$(CH$_3$)$_b$)$_2$]; 1.37 [d, J = 6 Hz, 12 H, −N(CH(CH$_3$)$_a$(C*H*$_3$)$_b$)$_2$]; 3.37 [s, 6 H, −N(C*H*$_3$)$_2$]; 3.45 [m, J = 6.4 Hz, 4 H, −N(C*H*(CH$_3$)$_a$(CH$_3$)$_b$)$_2$]. ^{13}C NMR (C$_6$D$_6$, 300 MHz): δ = 26.2 [−N(CH(*C*H$_3$)$_a$(CH$_3$)$_b$)$_2$]; 27.2 [−N(CH(*C*H$_3$)$_a$(CH$_3$)$_b$)$_2$]; 51.4 [−N(*C*H$_3$)$_2$]; 52.3 [−N(*C*H(CH$_3$)$_a$−(CH$_3$)$_b$)$_2$]. DIP-CI-MS: calcd for [M + H]$^+$ 443.2368; found 443.2364. $C_{14}H_{34}N_4W$ (442.29): calcd C 38.02, H 7.75, N 12.67; found C 37.89, H 7.68, N 12.63

*WN(NEt$_2$)$_2$(N^{i}Pr$_2$) (**8**).* In a 200 mL Schlenk flask, 0.50 g (1.5 mmol) of **1** and 80 mL of pentane were combined to form a white slurry. To the slurry, 6.0 mL of diisopropylamine (4.3 g, 43 mmol) was added to give an orange/red suspension. A reflux condenser was attached, and the mixture was brought to a gentle reflux under argon. After 12 h, solvent was removed from the amber/brown solution under vacuum at room temperature. The residue was extracted by stirring with hexamethyldisiloxane (50 mL) for 15 min and filtered through Celite. The filter pad was washed with additional hexamethyldisiloxane (2 × 5 mL). Solvent was removed from the resulting brown filtrate under vacuum to give crude **6**. This was dissolved in pentane (60 mL), and 3.0 mL of diethylamine (2.1 g, 29 mmol) was added. A reflux condenser was attached, and the mixture was brought to a gentle reflux under argon. After 12 h, solvent was removed from the dark brown solution under vacuum at room temperature. Sublimation of the crude residue (60−65 °C/200−300 mtorr) afforded 0.36 g (0.83 mmol) of pure **8** as a light amber microcrystalline powder (55%). ^{1}H NMR (C$_6$D$_6$, 300 MHz): δ = 1.15 [t, J = 7 Hz, 12 H, −N(CH$_2$C*H*$_3$)$_2$]; 1.34 [d, J = 6 Hz, 12 H, −N(CH(C*H*$_3$)$_2$)$_2$]; 3.42 [m, J = 6 Hz, 2 H, −N(C*H*(CH$_3$)$_2$)$_2$]; 3.51−3.72 [m, J = 7 Hz, 8 H, N(C*H*$_2$CH$_3$)$_2$]. ^{13}C NMR (C$_6$D$_6$, 300 MHz): δ = 17.6 [−N(CH$_2$*C*H$_3$)]; 26.6 [−N(CH(*C*H$_3$)$_2$)$_2$]; 51.2 [−N(*C*H$_2$CH$_3$)$_2$]; 52.7 [−N(*C*H(CH$_3$)$_2$)$_2$]. DIP-CI-MS: calcd for [M + H]$^+$ 443.2373; found 443.2366. $C_{14}H_{34}N_4W$ (442.29): calcd C 38.02, H 7.75, N 12.67; found C 37.79, H 7.71, N 12.58.

*WN(NEt$_2$)(N^{i}Pr$_2$)$_2$ (**9**).* In a 100 mL Schlenk flask, 0.50 g (1.5 mmol) of **1** and 10 mL of diisopropylamine (7.2 g, 71 mmol) were combined to create an orange/red suspension. A reflux condenser was attached, and the mixture was brought to a gentle reflux under argon. After 12 h, solvent was removed from the dark brown solution under vacuum at

dx.doi.org/10.1021/ja4117582 | J. Am. Chem. Soc. 2014, 136, 1650−1662

room temperature. The residue was extracted by stirring with hexamethyldisiloxane (50 mL) for 15 min and filtered through Celite. The filter pad was washed with additional hexamethyldisiloxane (2 × 5 mL). Solvent was removed from the resulting brown filtrate under vacuum to give crude **7**. This was dissolved in benzene (60 mL), and 3.0 mL of diethylamine (2.1 g, 29 mmol) was added. A reflux condenser was attached, and the mixture was brought to a gentle reflux under argon. After 12 h, solvent was removed from the dark brown solution under vacuum at room temperature. Sublimation of the crude product (60−65 °C/200−300 mtorr) afforded 0.35 g (0.75 mmol) of pure **9** as a light amber microcrystalline powder (50%). ^{1}H NMR (C_6D_6, 300 MHz): δ = 1.15 [t, J = 7 Hz, 6 H, −N(CH_2CH_3)$_2$]; 1.26 [d, J = 6 Hz, 12 H, −N(CH(CH_3)$_a$(CH_3)$_b$)$_2$]; 1.33 [br. d, 12 H, −N(CH-(CH_3)$_a$(CH_3)$_b$)$_2$]; 3.46 [m, J = 6 Hz, 4 H, −N(CH(CH_3)$_a$(CH_3)$_b$)$_2$]; 3.62 [q, J = 7 Hz, 4 H, −N(CH_2CH$_3$)$_2$]. ^{13}C NMR (C_6D_6, 300 MHz): δ = 17.2 [−N(CH_2CH_3)]; 26.8 [−N(CH(CH_3)$_a$(CH_3)$_b$)$_2$]; 51.4 [−N(CH_2CH_3)$_2$]; 52.7 [−N(CH(CH_3)$_a$−(CH_3)$_b$)$_2$]. DIP-CI-MS: calcd for [M + H]$^+$ 471.2687; found 471.2705. $C_{16}H_{38}N_4W$ (470.35): calcd C 40.86, H 8.14, N 11.91; found C 40.78, H 7.99, N 11.76.

*WN(O^{t}Bu)(N^{i}Pr$_2$)$_2$ (**10**).* In a 200 mL Schlenk flask, 1.71 g (2.94 mmol) of La(N^{i}Pr$_2$)$_3$·2THF and 100 mL of THF were combined to form a clear solution. To this solution, 1.75 g (4.19 mmol) of WN(O^{t}Bu)$_3$ was added all at once to create a golden-amber solution. The reaction flask was heated to 60 °C under Ar (initial darkening of the reaction mixture was observed, followed by an eventual return to golden-amber). After 24 h, solvent was removed under vacuum at room temperature to leave an amber residue. Pentane (50 mL) and diglyme (0.32 mL, 0.30 g, 2.2 mmol) were added, and the resulting slurry (off-white precipitate) was stirred for 1 h. The slurry was filtered through Celite, and the filter pad was washed with additional pentane (2 × 10 mL). Solvent was removed from the resulting amber filtrate under vacuum, and the solid amber residue was heated under vacuum (60−65 °C/200−300 mtorr) overnight. Sublimation (90−105 °C/200−300 mtorr) of the crude material overnight afforded 0.94 g (2.0 mmol) of pure **10** as a white microcrystalline powder (48%). ^{1}H NMR (25 °C, C_6D_6, 300 MHz): δ = 1.26 [br. s, 24 H, −N(CH-(CH_3)$_2$)$_2$]; 1.52 [s, 9 H, −OC(CH_3)$_3$]; 3.54 [m, J = 6 Hz, 4 H, −N(CH(CH_3)$_2$)$_2$]. ^{1}H NMR (75 °C, C_6D_6, 300 MHz): δ = 1.27 [d, J = 6 Hz, 12 H, −N(CH(CH_3)$_a$(CH_3)$_b$)$_2$]; 1.34 [d, J = 6 Hz, 12 H, −N(CH(CH_3)$_a$(CH_3)$_b$)$_2$]; 1.51 [s, 9 H, -OC(CH_3)$_3$]; 3.61 [m, J = 6 Hz, 4 H, −N(CH(CH_3)$_a$(CH_3)$_b$)$_2$]. ^{13}C NMR (75 °C, C_6D_6, 300 MHz): δ = 25.7 [−N(CH(CH_3)$_a$(CH_3)$_b$)$_2$]; 26.3 [−N(CH(CH_3)$_a$−(CH_3)$_b$)$_2$]; 32.6 [−OC(CH_3)$_3$]; 52.3 [−N(CH(CH_3)$_a$(CH_3)$_b$)$_2$]; 77.7 [−OC(CH_3)$_3$]. DIP-CI-MS: calcd for [M + H]$^+$ 472.2527; found 472.2514. $C_{16}H_{37}N_3OW$ (471.33): calcd C 40.77, H 7.91, N 8.92; found C 40.69, H 8.04, N 8.97.

*WN(N^{i}Pr$_2$)$_3$ (**11**).* In a 100 mL pressure flask, 1.23 g (11.5 mmol) of freshly prepared lithium diisopropylamide and 10 mL of diethyl ether were combined to form a clear solution. To this solution, 0.83 g (1.8 mmol) of **10** was added all at once to create a light amber solution. The pressure flask was sealed and immediately heated to 65 °C (the color of the reaction solution darkened initially and eventually became dark red/amber with tan precipitate). After 24 h, the pressure flask was returned to room temperature and solvent was removed under vacuum. The crude residue was extracted by stirring with pentane (100 mL) for 30 min and filtered through Celite. The filter pad was washed with additional pentane (2 × 10 mL). The resulting dark red/amber filtrate was concentrated to approximately 5 mL and placed in the glovebox freezer (−15 °C) overnight to yield 0.62 g of crude **11** as tan powder after removal of the mother liquor and drying under vacuum. The product was further purified by sublimation (115−125 °C/300−400 mtorr) overnight to yield 0.50 g (1.0 mmol) of pure **11** as a white microcrystalline powder (57%). ^{1}H NMR (25 °C, C_6D_6, 300 MHz): δ = 1.33 [br. s, 36 H, −N(CH(CH_3)$_2$)$_2$]; 3.50 [m, J = 6 Hz, 6 H, −N(CH(CH_3)$_2$)$_2$]. ^{1}H NMR (75 °C, C_6D_6, 300 MHz): δ = 1.34 [d, J = 6 Hz, 36 H, −N(CH(CH_3)$_2$)$_2$]; 3.56 [m, J = 6 Hz, 6 H, −N(CH(CH_3)$_2$)$_2$]. ^{13}C NMR (75 °C, C_6D_6, 300 MHz): δ = 26.4 [−N(CH(CH_3)$_2$)$_2$]; 51.7 [−N(CH(CH_3)$_2$)$_2$]. DIP-CI-MS: calcd for [M + H]$^+$ 499.3000; found 499.3027. $C_{18}H_{42}N_4W$ (498.40): calcd C 43.38, H 8.49, N 11.24; found C 43.43, H 8.56, N 11.28.

Substrate Preparation. The p-type boron-doped Si(100) substrates were acquired from Cemat Silicon and the n-type arsenic-doped Si(111) substrates from Crysteco. The wafers were cut to 1 cm × 1 cm, treated for 3 min each in boiling trichloroethylene, boiling acetone, and boiling methanol to remove any organic contamination on the surface, and subsequently rinsed for 30 s in boiling deionized water. Afterward, the substrates were placed in a buffered-oxide-etch (6:1 NH_4F:HF in water) for 2 min to remove the native surface oxide and leave a relatively air-stable hydrogen terminated surface. The samples were blown dry using 99.999% N_2, wiped with an acetone soaked lint-free alpha swab, and then blown dry again.

Film Growth. A custom built aerosol-assisted chemical vapor deposition reactor was used for the deposition studies, and is described elsewhere.[30] Precursor **1** was dissolved in pyridine at a concentration of 0.051 M and delivered at a rate of 4 mL/h and transported with 99.999% purity N_2 to the reaction zone through heated lines at 55 °C. This corresponds to a 3.40 × 10^{-6} mol/min precursor delivery rate, or approximately a 7.47 × 10^{-5} gas-phase mol fraction of precursor. The reactor operating pressure was maintained at 350 Torr, for bulk materials studies, with deposition temperatures ranging from 125 to 650 °C. The deposition time was 150 min.

Materials Characterization. The materials characterization was performed at the Major Analytical Instrumentation Center at the University of Florida. To ensure a high signal-to-noise ratio, GIXRD was employed in place of the traditional powder XRD. A Philips X'Pert MRD system was used to perform the X-ray diffraction scans using Cu Kα radiation with a scan rate of 0.03° 2θ per second. XRR measurements were also performed using this instrument with density information derived from the critical angle, θ_c, in the θ−2θ scans. XPS was performed using a Perkin-Elmer PHI 5100 ESCA System with an Al anode ($h\nu$ = 1486.3 eV) at 15 kV and 300 mA. The system had a nominal sputter rate of approximately 4 Å/min, and collected data were deconvoluted using the RBD Analysis suite of software. Pretreatment of samples involved sputtering for 20 min to remove surface contamination. This sputtering time was verified by collecting data after each minute of sputtering until compositional profiles became steady. A VEECO Dimension 3100 Atomic Force Microscope (AFM) was used to perform root-mean-square (RMS) surface roughness measurements. Typical measurements included a scan rate of 2 Hz with a resolution of 512 × 512 lines for a 2 μm × 6 μm area. An FEI XL-40 FESEM was used for imaging purposes with 20 kV as the accelerating voltage and 10 mm working distance.

Diffusion Barrier Testing. Complex **1** was used to deposit films for Cu diffusion barrier applications. 300 nm of MOCVD Cu was deposited onto freshly prepared (approximately 5 min of post-growth exposure to air) WN_xC_y/Si using (hfac)Cu^{I,II}(TMVS). The Cu/WN_xC_y/Si stack was subsequently annealed at a temperature of 500 °C for 30 min under a flow of 99.999% N_2. The annealed Cu/WN_xC_y/Si stacks were then analyzed by XRD, SEM, and 4PP. Etch-pit testing was performed by removing the Cu layer with a dilute nitric acid solution, then removing the barrier with a solution of NH_4OH, H_2O_2, and H_2O in a ratio of 1:1:4 for 10 min, followed by the etching of Cu_3Si for 5 s with Secco etchant [($K_2Cr_2O_7$:H_2O, 1:1):HF, 1:1].

■ ASSOCIATED CONTENT

Supporting Information

General experimental procedures. Modified procedures for synthesis of WN(O^{t}Bu)$_3$ and **1**. Procedures for thermolysis of **1** and **2**. Variable temperature ^{1}H NMR spectra for **7**, **9**, **10**, and **11**. X-ray experimental procedure, tables of crystal data and structural refinement, tables of bond distances, bond angles, positional parameters, and anisotropic displacement parameters for **2** and **7**. Experimental procedure for DFT calculations and tables of optimized Cartesian coordinates for decomposition pathways **A** and **B**. This material is available free of charge via the Internet at http://pubs.acs.org.

dx.doi.org/10.1021/ja4117582 | J. Am. Chem. Soc. 2014, 136, 1650−1662

AUTHOR INFORMATION

Corresponding Author
lmwhite@chem.ufl.edu

Notes
The authors declare no competing financial interest.

ACKNOWLEDGMENTS

We would like to thank the National Science Foundation for support under NSF Grant CHE-0911640. K.A.A. wishes to acknowledge the National Science Foundation and the University of Florida for funding of the purchase of the X-ray equipment. We would also like to thank the Major Analytical Instrumentation Center at the University of Florida for providing and maintaining materials characterization equipment.

REFERENCES

(1) ITRS International Technology Roadmap for Semiconductors: 2011 ed., International SEMATECH, 2011.
(2) Lee, C.; Kuo, Y. L. *JOM* **2007**, *59*, 44.
(3) Singer, P. *Semicond. Int.* **2006**, *29*, 32.
(4) Kaloyeros, A. E.; Eisenbraun, E. *Annu. Rev. Mater. Sci.* **2000**, *30*, 363.
(5) Rossnagel, S. M.; Hopwood, J. *Appl. Phys. Lett.* **1993**, *63*, 3285.
(6) ITRS. Emerging Research Materials Difficult Challenges. [Online Early Access]. Published Online: 2011. http://www.itrs.net/Links/2011ITRS/2011Chapters/2011ERM.pdf.
(7) Kafizas, A.; Carmalt, C. J.; Parkin, I. P. *Coord. Chem. Rev.* **2013**, *257*, 2073.
(8) Holloway, K.; Fryer, P. M.; Cabral, C., Jr.; Harper, J. M. E.; Bailey, P. J.; Kelleher, K. H. *J. Appl. Phys.* **1992**, *71*, 5433.
(9) Chiu, H. T.; Chang, W. P. *J. Mater. Sci. Lett.* **1992**, *11*, 96.
(10) Tsai, M. H.; Sun, S. C.; Chiu, H. T.; Tsai, C. E.; Chuang, S. H. *Appl. Phys. Lett.* **1995**, *67*, 1128.
(11) Min, K.-H.; Chun, K.-C.; Kim, K.-B. *J. Vac. Sci. Technol., B* **1996**, *14*, 3263.
(12) Tsai, M. H.; Sun, S. C.; Tsai, C. E.; Chuang, S. H.; Chiu, H. T. *J. Appl. Phys.* **1996**, *79*, 6932.
(13) Cho, S.-L.; Kim, K.-B.; Min, S.-H.; Shin, H.-K. *Mater. Res. Soc. Symp. Proc.* **1998**, *514*, 531.
(14) Chen, X.; Peterson, G. G.; Goldberg, C.; Nuesca, G.; Frisch, H. L.; Kaloyeros, A. E.; Arkles, B.; Sullivan, J. *J. Mater. Res.* **1999**, *14*, 2043.
(15) Kaloyeros, A. E.; Chen, X. M.; Stark, T.; Kumar, K.; Seo, S.; Peterson, G. G.; Frisch, H. L.; Arkles, B.; Sullivan, J. *J. Electrochem. Soc.* **1999**, *146*, 170.
(16) Chen, T.; Xu, C.; Baum, T. H.; Stauf, G. T.; Roeder, J. F.; DiPasquale, A. G.; Rheingold, A. L. *Chem. Mater.* **2010**, *22*, 27.
(17) Yun, J. Y.; Park, M. Y.; Rhee, S. W. *J. Electrochem. Soc.* **1999**, *146*, 1804.
(18) Cheung, N.; Vonseefeld, H.; Nicolet, M. A. *J. Electrochem. Soc.* **1979**, *126*, C346.
(19) Kurtz, S. R.; Gordon, R. G. *Thin Solid Films* **1986**, *140*, 277.
(20) Sherman, A. *J. Electrochem. Soc.* **1990**, *137*, 1892.
(21) Winter, C. H.; Sheridan, P. H.; Lewkebandara, T. S.; Heeg, M. J.; Proscia, J. W. *J. Am. Chem. Soc.* **1992**, *114*, 1095.
(22) Musher, J. N.; Gordon, R. G. *J. Electrochem. Soc.* **1996**, *143*, 736.
(23) Min, J.-S.; Son, Y.-W.; Kang, W.-G.; Chun, S.-S.; Kang, S.-W. *Jpn. J. Appl. Phys., Part 1* **1998**, *37*, 4999.
(24) Kim, S. H.; Kim, J. K.; Lee, J. H.; Kwak, N.; Kim, J.; Jung, S. H.; Hong, M. R.; Lee, S. H.; Collins, J.; Sohn, H. *J. Electrochem. Soc.* **2007**, *154*, D435.
(25) Nakajima, T.; Watanabe, K.; Watanabe, N. *J. Electrochem. Soc.* **1987**, *134*, 3175.
(26) Chiu, H. T.; Chuang, S. H. *J. Mater. Res.* **1993**, *8*, 1353.
(27) Kelsey, J. E.; Goldberg, C.; Nuesca, G.; Peterson, G.; Kaloyeros, A. E.; Arkles, B. *J. Vac. Sci. Technol., B* **1999**, *17*, 1101.
(28) Becker, J. S.; Suh, S.; Wang, S.; Gordon, R. G. *Chem. Mater.* **2003**, *15*, 2969.
(29) Bchir, O. J.; Green, K. M.; Hlad, M. S.; Anderson, T. J.; Brooks, B. C.; Wilder, C. B.; Powell, D. H.; McElwee-White, L. *J. Organomet. Chem.* **2003**, *684*, 338.
(30) Bchir, O. J.; Johnston, S. W.; Cuadra, A. C.; Anderson, T. J.; Ortiz, C. G.; Brooks, B. C.; Powell, D. H.; McElwee-White, L. *J. Cryst. Growth* **2003**, *249*, 262.
(31) Bchir, O. J.; Green, K. M.; Ajmera, H. M.; Zapp, E. A.; Anderson, T. J.; Brooks, B. C.; Reitfort, L. L.; Powell, D. H.; Abboud, K. A.; McElwee-White, L. *J. Am. Chem. Soc.* **2005**, *127*, 7825.
(32) Dezelah, C. L.; El-Kadri, O. M.; Kukli, K.; Arstila, K.; Baird, R. J.; Lu, J.; Niinisto, L.; Winter, C. H. *J. Mater. Chem.* **2007**, *17*, 1109.
(33) Ajmera, H. M.; Anderson, T. J.; Koller, J.; McElwee-White, L.; Norton, D. P. *Thin Solid Films* **2009**, *517*, 6038.
(34) Kim, H. *J. Vac. Sci. Technol., B* **2003**, *21*, 2231.
(35) Ritala, M.; Kalsi, P.; Riihelae, D.; Kukli, K.; Leskelae, M.; Jokinen, J. *Chem. Mater.* **1999**, *11*, 1712.
(36) Juppo, M.; Ritala, M.; Leskela, M. *J. Electrochem. Soc.* **2000**, *147*, 3377.
(37) Cho, S. L.; Kim, K. B.; Min, S. H.; Shin, H. K.; Kim, S. D. *J. Electrochem. Soc.* **1999**, *146*, 3724.
(38) Park, K. C.; Kim, K. B. *J. Electrochem. Soc.* **1995**, *142*, 3109.
(39) Park, K. C.; Kim, K. B. *Mater. Res. Soc. Symp. Proc.* **1995**, *391*, 211.
(40) Park, K. C.; Kim, K. B.; Raaijmakers, I.; Ngan, K. *J. Appl. Phys.* **1996**, *80*, 5674.
(41) Casey, P.; Bogan, J.; McCoy, A.; Lozano, J. G.; Nellist, P. D.; Hughes, G. *J. Appl. Phys.* **2012**, 112.
(42) Sun, H. Q.; Qin, X. D.; Zaera, F. *J. Phys. Chem. Lett.* **2011**, *2*, 2525.
(43) Matsumoto, K.; Neishi, K.; Itoh, H.; Sato, H.; Hosaka, S.; Koike, J. *Appl. Phys. Express* **2009**, 2.
(44) Moon, D. Y.; Han, D. S.; Park, J. H.; Shin, S. Y.; Park, J. W.; Kim, B. M.; Cho, J. Y. *Thin Solid Films* **2012**, *521*, 146.
(45) Au, Y.; Lin, Y. B.; Kim, H.; Beh, E.; Liu, Y. Q.; Gordon, R. G. *J. Electrochem. Soc.* **2010**, *157*, D341.
(46) Lee, B. H.; Yong, K. *J. Vac. Sci. Technol., B: Microelectron. Nanometer Struct.–Process., Meas., Phenom.* **2004**, *22*, 2375.
(47) Suh, B. S.; Lee, Y. J.; Hwang, J. S.; Park, C. O. *Thin Solid Films* **1999**, *348*, 299.
(48) Uekubo, M.; Oku, T.; Nii, K.; Murakami, M.; Takahiro, K.; Yamaguchi, S.; Nakano, T.; Ohta, T. *Thin Solid Films* **1996**, *286*, 170.
(49) Koh, W.; Kumar, D.; Li, W. M.; Sprey, H.; Raaijmakers, I. J. *Solid State Technol.* **2005**, *48*, 54.
(50) Kim, S.-H.; Oh, S. S.; Kim, H.-M.; Kang, D.-H.; Kim, K.-B.; Li, W.-M.; Haukka, S.; Tuominen, M. *J. Electrochem. Soc.* **2004**, *151*, C272.
(51) Kim, D.; Kim, O. H.; Ajmera, H. M.; Anderson, T.; Koller, J.; Abboud, K. A.; McElwee-White, L. *J. Electrochem. Soc.* **2011**, *158*, H618.
(52) Gwildies, V.; Thiede, T. B.; Amirjalayer, S.; Alsamman, L.; Devi, A.; Fischer, R. A. *Inorg. Chem.* **2010**, *49*, 8487.
(53) Ajmera, H. M.; Heitsch, A. T.; Anderson, T. J.; Wilder, C. B.; Reitfort, L. L.; McElwee-White, L.; Norton, D. P. *J. Vac. Sci. Technol., B* **2008**, *26*, 1800.
(54) Rische, D.; Parala, H.; Gemel, E.; Winter, M.; Fischer, R. A. *Chem. Mater.* **2006**, *18*, 6075.
(55) Becker, J. S.; Gordon, R. G. *Appl. Phys. Lett.* **2003**, *82*, 2239.
(56) Anacleto, A. C.; Blasco, N.; Pinchart, A.; Marot, Y.; Lachaud, C. *Surf. Coat. Technol.* **2007**, *201*, 9120.
(57) Li, W.-M. *Chem. Vap. Deposition* **2013**, *19*, 82.
(58) Zeng, W.; Wang, X.; Kumar, S.; Peters, D. W.; Eisenbraun, E. T. *J. Mater. Res.* **2007**, *22*, 703.
(59) McElwee-White, L.; Koller, J.; Kim, D.; Anderson, T. J. *ECS Trans.* **2009**, *25*, 161.
(60) McElwee-White, L. *Dalton Trans.* **2006**, 5327.
(61) Potts, S. E.; Carmalt, C. J.; Blackman, C. S.; Leese, T.; Davies, H. O. *Dalton Trans.* **2008**, 5730.
(62) Koller, J.; Ajmera, H. M.; Abboud, K. A.; Anderson, T. J.; McElwee-White, L. *Inorg. Chem.* **2008**, *47*, 4457.
(63) McClain, K. R.; O'Donohue, C.; Shi, Z.; Walker, A. V.; Abboud, K. A.; Anderson, T.; McElwee-White, L. *Eur. J. Inorg. Chem.* **2012**, *2012*, 4579.
(64) Aspinall, H. C.; Tillotson, M. R. *Polyhedron* **1994**, *13*, 3229.

(65) Kumar, N.; Yang, Y.; Noh, W.; Girolami, G. S.; Abelson, J. R. *Chem. Mater.* **2007**, *19*, 3802.
(66) Clough, C. R.; Greco, J. B.; Figueroa, J. S.; Diaconescu, P. L.; Davis, W. M.; Cummins, C. C. *J. Am. Chem. Soc.* **2004**, *126*, 7742.
(67) DiFranco, S. A.; Maciulis, N. A.; Staples, R. J.; Batrice, R. J.; Odom, A. L. *Inorg. Chem.* **2011**, *51*, 1187.
(68) Firman, T. K.; Landis, C. R. *J. Am. Chem. Soc.* **2001**, *123*, 11728.
(69) Lewkebandara, T. S.; Sheridan, P. H.; Heeg, M. J.; Rheingold, A. L.; Winter, C. H. *Inorg. Chem.* **1994**, *33*, 5879.
(70) Amato, C. C.; Hudson, J. B.; Interrante, L. V. *Mater. Res. Soc. Symp. Proc.* **1990**, *168*, 119.
(71) Chae, Y.; Houf, W. G.; McDaniel, A. H.; Troup, J.; Allendorf, M. D. *J. Electrochem. Soc.* **2004**, *151*, C527.
(72) Chae, Y.; Houf, W. G.; McDaniel, A. H.; Allendorf, M. D. *J. Electrochem. Soc.* **2006**, *153*, C309.
(73) Sun, S. C. In *Solid-State and Integrated Circuit Technology Proceedings*; IEEE, 1998; pp 243−246.
(74) Choy, K. L. *Prog. Mater. Sci.* **2003**, *48*, 57.
(75) Chen, H.; Yang, Y.; Hu, Z.; Huo, K. F.; Ma, Y. W.; Chen, Y.; Wang, X. S.; Lu, Y. N. *J. Phys. Chem. B* **2006**, *110*, 16422.
(76) Kreuzer, H. J. *J. Chem. Phys.* **1996**, *104*, 9593.
(77) *NIST X-ray Photoelectron Spectroscopy Database*, Version 4.1; National Institute of Standards and Technology: Gaithersburg, MD, 2012; http://srdata.nist.gov/xps/.
(78) Ajmera, H. M.; Heitsch, A. T.; Bchir, O. J.; Anderson, T. J.; Reitfort, L. L.; McElwee-White, L. *J. Electrochem. Soc.* **2008**, *155*, H829.
(79) Kim, D.; Kim, O. H.; Anderson, T.; Koller, J.; McElwee-White, L.; Leu, L. C.; Tsai, J. M.; Norton, D. P. *J. Vac. Sci. Technol., A* **2009**, *27*, 943.
(80) Karpenko, O. P.; Yalisove, S. M.; Eaglesham, D. J. *J. Appl. Phys.* **1997**, *82*, 1157.
(81) Chevrier, J.; Cruz, A.; Pinto, N.; Berbezier, I.; Derrien, J. *J. Phys. I* **1994**, *4*, 1309.
(82) Takahashi, K.; Nakayama, M.; Yokoyama, S.; Kimura, T.; Tokumitsu, E.; Funakubo, H. *Appl. Surf. Sci.* **2003**, *216*, 296.
(83) Abom, A. E.; Haasch, R. T.; Hellgren, N.; Finnegan, N.; Hultman, L.; Eriksson, M. *J. Appl. Phys.* **2003**, *93*, 9760.
(84) Israelachvili, J.; Maeda, N.; Rosenberg, K. J.; Akbulut, M. *J. Mater. Res.* **2005**, *20*, 1952.
(85) Ferrari, A. C.; Libassi, A.; Tanner, B. K.; Stolojan, V.; Yuan, J.; Brown, L. M.; Rodil, S. E.; Kleinsorge, B.; Robertson, J. *Phys. Rev. B* **2000**, *62*, 11089.
(86) Suetin, D. V.; Shein, I. R.; Ivanovskii, A. L. *J. Struct. Chem.* **2009**, *50*, 1.
(87) Hoyas, A. M.; Travaly, Y.; Schuhmacher, J.; Sajavaara, T.; Whelan, C. M.; Eyckens, B.; Richard, O.; Giangrandi, S.; Brijs, B.; Vandervorst, W.; Maex, K.; Celis, J. P.; Jonas, A. M.; Vantomme, A. *J. Appl. Phys.* **2006**, 99.
(88) Marcus, S. D.; Foster, R. F. *Thin Solid Films* **1993**, *236*, 330.
(89) Volders, H.; Tokei, Z.; Bender, H.; Brijs, B.; Caluwaerts, R.; Carbonell, L.; Conard, T.; Drijbooms, C.; Franquet, A.; Garaud, S.; Hoflijk, I.; Moussa, A.; Sinapi, F.; Travaly, Y.; Vanhaeren, D.; Vereecke, G.; Zhao, C.; Li, W. M.; Sprey, H.; Jonas, A. M. *Microelectron. Eng.* **2007**, *84*, 2460.
(90) Kim, S. H.; Chung, D. S.; Park, K. C.; Kim, K. B.; Min, S. H. *J. Electrochem. Soc.* **1999**, *146*, 1455.
(91) Shacham-Diamand, Y. *J. Electron. Mater.* **2001**, *30*, 336.
(92) Yang, D.; Hong, J.; Richards, D.; Cale, T. *J. Vac. Sci. Technol., B* **2002**, *20*, 495.
(93) Kroger, R.; Eizenberg, M.; Cong, D.; Yoshida, N.; Chen, L.; Ramaswami, S.; Carl, D. *J. Electrochem. Soc.* **1999**, *146*, 3248.